Investigating Clutter Reduction for Unmanned Systems Applications using Imaging Polarimetry

Jonathan B. Hanks, Todd M. Aycock, David B. Chenault
Polaris Sensor Technologies, Inc. 200 Westside Square, Suite 320, Huntsville, AL 35801

ABSTRACT

The proliferation of unmanned systems in recent years has sparked increased interest in multiple areas of research for on-board image processing including autonomous navigation, surveillance, detection, and tracking to name a few. For these applications, techniques for reducing scene clutter provide an increased level of robustness for autonomous systems and reduced operator burden for tele-operated systems. Because imaging polarimetry frequently provides complementary information to the standard radiometric image, it is anticipated that this technology is well suited to provide a significant reduction in scene clutter. In this paper, the authors investigate the use of imaging polarimetry under a number of representative scenarios to assess the utility of this technology for unmanned system applications.

Keywords: Polarimetry, Polarization, IR Imaging, Improved Contrast, Unmanned Systems

1. INTRODUCTION

The utilization of unmanned vehicles as a force multiplier has resulted in an ever expanding number of operation spaces for these platforms. Consequently, there is an increased need to expand the performance capabilities of the on-board sensor suite while maintaining low size, weight, power, and cost (SWaP-C). The advent of microbolometer technology in recent years has resulted in a low SWaP-C thermal imager that is well suited for numerous unmanned applications. While the capabilities of these sensors is clearly evident, thermal imagers have traditionally demonstrated poor performance in cluttered scenes where large portions of the image are in thermal equilibrium. In the thermal infrared, cases of thermal equilibrium between objects results in a loss of contrast, making complex scenes difficult to interpret. Passive Long Wave Infrared (LWIR) imaging polarimetry is an appealing solution as it provides additional scene contrast without sacrificing the standard thermal image[1].

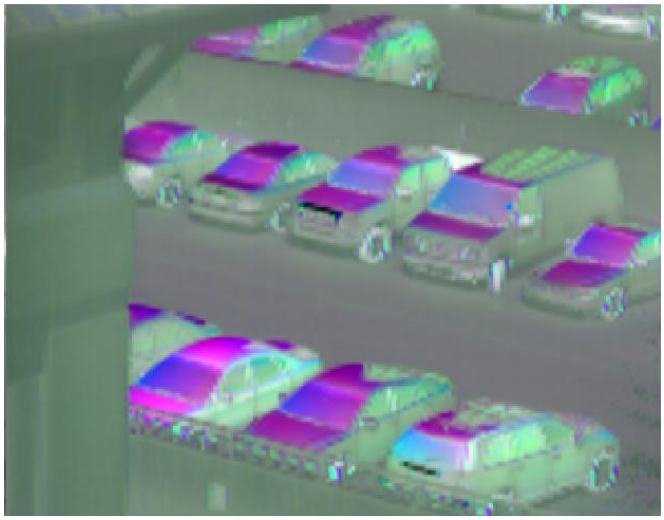

Figure 1. Enhancement of thermal imagery using polarization-based color queuing

It has been well established in the literature that imaging LWIR polarimetry provides a robust method for recovering contrast in scenes with low thermal variation[2]. Polarimetric signatures have been shown to be stable throughout the diurnal cycle including demonstrating particular utility during instances of thermal cross-over[3]. Because it is fundamentally a physics-based approach for recovering image contrast, imaging polarimetry is particularly adept at distinguishing between man-made and naturally-occurring objects[4,5,6,7]. This paper seeks to demonstrate infrared imaging polarimetry's capability to reduce clutter in complex thermal scenes. Specific interest is given to the microbolometer-based polarimeters due to their capability to deliver optimum performance while maintaining low SWaP-C. Presented here-in are numerous scenarios that demonstrate polarimetry's ability to augment the standard thermal image with particular consideration for unmanned applications including autonomous platforms, tele-operation, and Intelligence, Surveillance, Reconnaissance (ISR). These results may be achieved through any number of architectures to sense infrared polarization.

2. REVIEW OF POLARIMETRY

Polarization results from the vector nature of light. As light propagates along a given vector, the electric field oscillates sinusoidally along an axis that is orthogonal to the propagation axis, as described by the wave equation[8]. This oscillation can be described using four parameters: 1) the amplitude of the oscillation (i.e. the intensity), 2) the spacing between the peaks of the oscillation (i.e. wavelength), 3) the coherence of the oscillation, and 4) the angle between the axis of oscillation and horizontal axis (i.e. the polarization angle), as shown in **Figure 2**. Polarization is therefore a fundamental quantity of the propagating light wave just as intensity, wavelength, and coherence are also fundamental quantities.

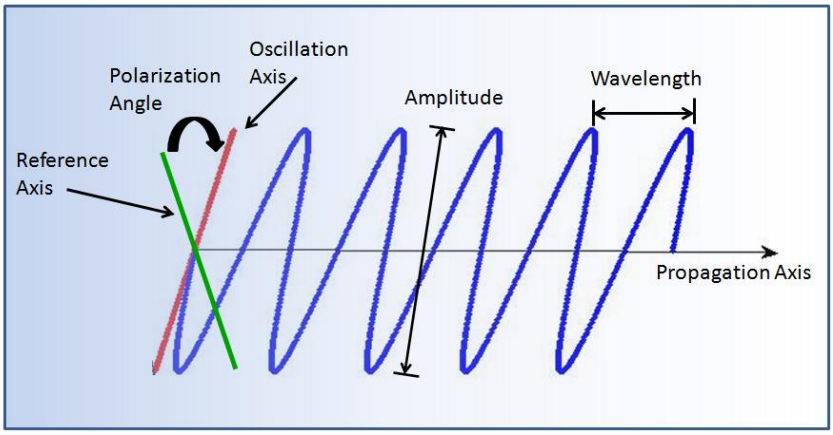

Figure 2. Polarization of propagating light wave

As the wave interacts with a surface boundary (whether through reflection or emission), the surface preferentially passes one orientation of the e-field. Similarly the same surface will preferentially attenuate the orthogonal e-field orientation. The combination of these two actions produces polarized light. For emission, the surface preferentially emits an e-field that oscillates parallel to the surface normal (the opposite is true for reflection)[9]. The degree of preferential emission and preferential attenuation (i.e. the degree of polarization) is dependent on the smoothness of the surface and the angle of incidence (AOI) between the incident light and the surface[10]. Thus, for a polarimetric image, contrast between two surfaces occurs when there is a change in the surface roughness and/or AOI relative to the sensor. Comparison of example thermal and polarimetric images are presented in **Section 4**.

As the oscillation of the e-field can be described using a vector, it is therefore possible to decompose that vector into its two orthogonal components. Typically, the orthogonal components used are the horizontal (parallel to the earth's surface) and vertical (perpendicular to the earth's surface). The comparison of horizontal and vertical is referred to as the S1 parameter. Because S1 is based on a comparison of horizontal and vertical, there are three special cases to consider: 1) all light is polarized at 45^{o}, 2) all light is polarized at 135^{o}, and 3) all light is equally distributed across all possible orientations (i.e. unpolarized light). Each of these three cases will produce

an S1 value of zero, even though the light is completely polarized in cases 1 and 2. To address this, a second standard parameter is used to compare 45° and 135° light, referred to as the S2 parameter. Finally, the standard radiometric image is therefore simply the summation of orthogonal components from either S1 or S2.

Put together, the S_0, S_1, and S_2 parameters (collectively referred to as Stokes Parameters) provide a complete description of the orientation and amplitude of the incident thermal energy. One additional parameter, the Degree of Linear Polarization (DoLP), combines all the available polarimetric information into a single value. For the purposes of this paper, DoLP will serve as the polarimetric data product of interest for comparing polarimetry to the standard radiometric image. The functional form for these polarimetric data products can be found in **Equations (1)** through **(4)**.

$$\textit{Thermal Image} = S_0 = H + V = 45 + 135 = .5 \cdot (H + 45 + V + 135) \quad \textbf{(1)}$$

$$S_1 = (H - V)/(H + V) = (H - V)/S_0 \quad \textbf{(2)}$$

$$S_2 = (45 - 135)/(45 + 135) = (45 - 135)/S_0 \quad \textbf{(3)}$$

$$DoLP = \sqrt{S_1^2 + S_2^2} \quad \textbf{(4)}$$

3. INFRARED IMAGING POLARIMETERS

There are several different architectures, or design approaches, for collecting infrared polarimetric imagery. Polaris Sensor Technologies has an extremely wide range of these architectures available as commercial off the shelf cameras / sensor systems. The choice of one particular architecture over another has much to do with the desired polarimetric accuracy/resolution, the electronic processing capability available, and the SWaP-C constraints. In general, the results that we present throughout this paper are achievable using any one of our COTS sensors so that the choice of sensor for a particular application is truly driven by those factors just mentioned.

While S_0 is the standard thermal image and reports changes in intensity, the other three polarimetric data products can be regarded as a variation on Michelson's Contrast Formula and thus produce image contrast that is not dependent on intensity[11]. For this reason, the contrast obtained from S_1, S_2, and/or DoLP can be fused with the thermal image to create an Enhanced Thermal (eTherm™) image that leverages all available information to generate a more-complete representation of the scene. Because S_0, S_1, S_2, and DoLP are all generated simultaneously for each output frame, the eTherm image is therefore simultaneously generated as well.

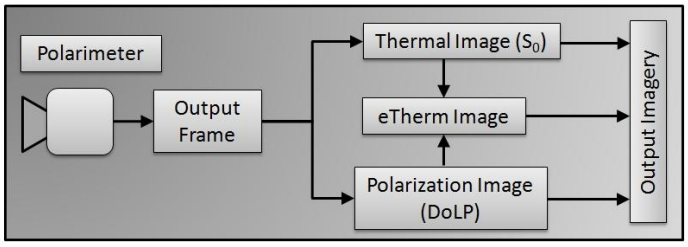

Figure 3. Simultaneous capture of thermal, polarization, and eTherm imagery

4. RECOVERY OF CONTRAST

The following figures and tables present numerous scenarios that demonstrate the utility of imaging LWIR polarimetry to augment the standard thermal image. The reader is reminded that imaging polarimeters capture both the polarimetric data product and the standard thermal image simultaneously. All data is organized into a standard format showing a visible reference image on the left, the standard thermal image (S_0) in the middle, and

the DoLP image on the right. Regions of Interest (ROI's) are denoted in the visible image, and spatial averages for each corresponding ROI in the thermal and DoLP images are presented in an accompanying table. The figures are intended to provide the reader with a qualitative comparison of the thermal and polarimetric image, with the tables providing the necessary quantitative scientific data. The polarimeter was calibrated with a laboratory blackbody using a standard multi-point non-uniformity correction method to produce thermal images in radiometric units (Watts/Centimeter^2/Steradian)[12]. As per **Equation (4)**, DoLP has normalized units. In order to present the data fairly, the images are displayed with upper and lower bounds derived from image statistics as per **Equations (5)** and **(6)**, where "$\langle\ \rangle$" denotes a spatial operation with both the thermal and DoLP images utilize a common "α" multiplier. In the following tables we will demonstrate that with the polarimetric image, the improvement in target contrast is such that even a simple thresholding scheme is sufficient to identify targets of interest, such as vehicles, with a high polarization value. For the purposes of this paper the "Threshold" value presented in the accompanying tables is calculated as per **Equation (7)**. In this way, the threshold value is driven by the statistics of the scene, rather than an arbitrary threshold value.

$$Lower-Bound = Mean\langle \mathrm{Im}age\rangle - \alpha \cdot StDev\langle \mathrm{Im}age\rangle \quad \textbf{(5)}$$

$$Upper-Bound = Mean\langle \mathrm{Im}age\rangle + \alpha \cdot StDev\langle \mathrm{Im}age\rangle \quad \textbf{(6)}$$

$$Threshold = Mean\langle \mathrm{Im}age\rangle + 2 \cdot StDev\langle \mathrm{Im}age\rangle \quad \textbf{(7)}$$

Figure 4, shown below, presents a group of cars cast in shadow on three sides from a surrounding parking structure. The vehicles have been allowed to reach near thermal equilibrium with the surrounding area to demonstrate minimum contrast in the thermal image (center). Comparatively, the DoLP image (right) shows excellent recovery of contrast of the vehicles. Spatial averages of the various ROI's can be found in **Table 1** for both the thermal and polarimetric imagery. Note that even though the area surrounding the vehicle has a low average contrast in both images, the contrast between the windshield and the frame is almost an order of magnitude higher in the DoLP frame versus the thermal image. Note that in the thermal image the windshield is below the threshold value, but by contrast the windshield is well above the DoLP threshold.

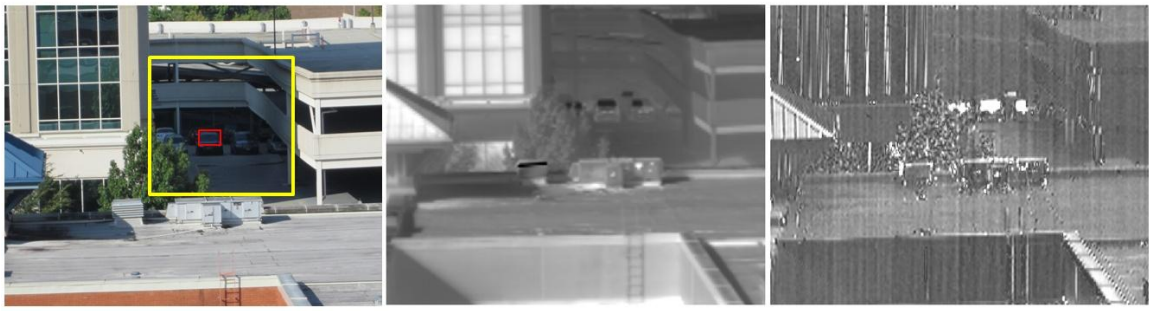

Figure 4. Vehicles at thermal equilibrium with surroundings shown in the visible reference image (left), standard thermal image (middle), and polarimetric image (right).

Table 1. Spatial average measurements from Figure 4 ROI's

Region of Interest	Description	S0 (W/cm2/Sr)	DoLP
Entire FOV	Image Mean	0.001383	0.0144
Entire FOV	Image St.Dev.	0.000125	0.0082
Entire FOV	Threshold Value	0.001633	0.0309
Yellow Box	Surrounding Area	0.001278	0.0134
Red Box	Windshield	0.001178	0.0855

Unlike shadows in the visible waveband, thermal shadows are a more persistent signature because they remain observable until the shadowed region returns to thermal equilibrium with its surroundings. ROI's 1, 2, 5 and 6 in **Figure 5**, below, demonstrate thermal shadows at various stages of imbalance with the surrounding scene. By comparison, because the DoLP data product is intensity-independent, thermal shadow signatures are mitigated, resulting in image contrast between surfaces with different textures. The DoLP signature is highly influenced by surface roughness; in this instance the vehicle surface is much smoother than the surrounding pavement. Note that in the thermal image, none of vehicles are above the threshold value, whereas all three vehicles are well above the DoLP threshold value.

Figure 5. Mitigation of thermal shadows using polarimetry illustrated in the visible reference image (left), standard thermal image (middle), and polarimetric image (right).

Table 2. Quantitative measurements from Figure 5 ROI's

Region of Interest #	Description	S0 (W/cm2/Sr)	DoLP
Entire FOV	Image Mean	0.001659	0.0116
Entire FOV	Image St.Dev.	0.000081	0.0112
Entire FOV	Threshold Value	0.001821	0.0339
1	Thermal Shadow 1	0.001580	0.0064
2	Thermal Shadow 2	0.001649	0.0083
3	Car 1	0.001775	0.0352
4	Thermal Shadow 3	0.001675	0.0092
5	Thermal Shadow 4	0.001566	0.0083
6	Car 2	0.001714	0.0471
7	Car 3	0.001780	0.0423
8	Pavement	0.001747	0.0127

Figure 6, below, shows a pedestrian walking across a roadway to a vehicle in shadow underneath a tree. As with the previous figure, polarimetry demonstrates a robust capability at recovering contrast with objects in thermal equilibrium with its surroundings. Furthermore, note that the pedestrian, the tree canopy, and the vehicle all have similar radiometric values (see **Table 3**). However, the vehicle produces a much higher DoLP signature compared to the pedestrian and the tree canopy. This is to be expected given polarimetry's propensity to detect man-made objects against natural backgrounds. Furthermore, this data demonstrates polarimetry's ability to discriminate between vehicles and pedestrians. Note that even in shadow, the vehicle exceeds the DoLP threshold value, whereas the vehicle is well below the threshold value in the thermal image.

Figure 6. Pedestrian and vehicle in shadow shown in the visible reference image (left), standard thermal image (middle), and polarimetric image (right).

Table 3. Spatial average measurements from Figure 6 ROI's

Region of Interest #	Description	S0 (W/cm2/Sr)	DoLP
Entire FOV	Image Mean	0.001627	0.0089
Entire FOV	Image St.Dev.	0.000097	0.0039
Entire FOV	Threshold Value	0.001821	0.0167
1	Pavement (Direct Sun)	0.001781	0.0128
2	Pavement (Shadowed)	0.001574	0.0069
3	Pedestrian	0.001583	0.0060
4	Tree Canopy	0.001525	0.0042
5	Car in Shadow	0.001569	0.0198

While the previous figures have dealt with overcoming shadowing effects, **Figure 7** illustrates polarimetry's ability to reduce clutter in full-sun scenes. Here, two vehicle are obscured by tree canopy (ROI's 2 and 4) and are at near thermal equilibrium with the surrounding pavement. By comparison, the DoLP image is able to clearly distinguish the vehicles, roadway, and trees, thus reducing scene clutter. Note that the cars are just below the threshold value in the thermal image, but roughly twice the threshold value in the DoLP image. As such, this data shows the robustness of the DoLP contrast enhancement regardless of whether or not the target is in shadow or direct sun.

Figure 7. Detection of vehicles obscured by trees illustrated in the visible reference image (left), standard thermal image (middle), and polarimetric image (right).

Table 4. Quantitative measurements from Figure 7 ROI's

Region of Interest #	Description	S0 (W/cm2/Sr)	DoLP
Entire FOV	Image Mean	0.001563	0.0075
Entire FOV	Image St.Dev.	0.000082	0.0056
Entire FOV	Threshold Value	0.001727	0.0187
1	Obscuring Tree	0.001512	0.0059
2	Roadway	0.001690	0.0112
3	Car 1	0.001707	0.0318
4	Car 2	0.001645	0.0204

As shown earlier, polarimetry's ability to recover image contrast is in part a function of the surface texture independent of the thermal intensity. A complex scene is presented in **Figure 8**, containing a roadway, gravel, and train tracks, all of which have a shadow extending over the entire FOV. As with the previous figures, the change in texture between these three surfaces results in a recovery of contrast in the DoLP image while simultaneously mitigating the shadow signature. Furthermore, note that the polarimetric image also provides improved detection of the vehicles along the roadway. Note that the thresholding allows for separation of the roadway and the train tracks from the surround gravel (shadowed and direct sun) in the DoLP image, whereas only the gravel directly illuminated by the sun is above the threshold value for the thermal image.

Figure 8. Shadow extended across train tracks and roadway shown in the visible reference image (left), standard thermal image (middle), and polarimetric image (right).

Table 5. Quantitative measurements from Figure 8 ROI's

Region of Interest #	Description	S0 (W/cm2/Sr)	DoLP
Entire FOV	Image Mean	0.001306	0.0048
Entire FOV	Image St.Dev.	0.000074	0.0221
Entire FOV	Threshold Value	0.001454	0.0490
1	Roadway (Direct Sun)	0.001451	0.0428
2	Roadway (Shadowed)	0.001395	0.0443
3	Gravel (Direct Sun)	0.001523	0.0139
4	Gravel (Shadowed)	0.001387	0.0144
5	Train Track	0.001329	0.1609
6	Car (Top Left)	0.001328	0.1274

Lastly, **Figure 9** is presented as it is the most complex scene, containing an amalgamation of all examples discussed in the previous figures. Here, a nighttime scene recorded at 10:45 pm results in low thermal contrast between trees, poles, and the surrounding pavement. Furthermore, dark patches can be observed in the parking lot, some of which are persistent thermal shadows while others are cold sky-shine reflected off vehicle windshields in thermal equilibrium with the surrounding pavement. The clutter of this scene is shown to be significantly reduced in the DoLP image; eliminating the thermal shadows, highlighting the highly polarized vehicles, and recovering contrast between the roadway and the trees (ROI's 1 and 2). Note again that both vehcile are above the threshold value in the DoLP image where as neither

Figure 9. Recovery of contrast in polarimetric image in low light conditions illustrated in the visible reference image (left), standard thermal image (middle), and polarimetric image (right).

Table 6 Quantitative measurements from Figure 9 ROI's

Region of Interest #	Description	S0 (W/cm2/Sr)	DoLP
Entire FOV	Image Mean	0.001227	0.0214
Entire FOV	Image St.Dev.	0.000052	0.0079
Entire FOV	Threshold Value	0.001331	0.0372
1	Tree	0.001207	0.0211
2	Roadway	0.001238	0.0307
3	Pavement (Thermal Shadow)	0.001210	0.0252
4	Pavement (No Shadow)	0.001295	0.0223
5	Truck 1	0.001115	0.0516
6	Truck 2	0.001107	0.0693

5. COLOR QUEUING USING ETHERM

In the previous section, thermal and polarimetric data was presented to aid the reader in making a side-by-side comparison between the two data products. However, for man-in-the-loop applications, this is not necessarily practical. To ensure operator burden is minimized, a method is needed to easily impart thermal and polarimetric information into a single image. Using a fusion algorithm developed by Polaris Sensor Technologies, polarimetric data can be used to colorize the thermal image. In this way, the intensity information in the thermal image is preserved, while the polarization-based coloring aids the operator in interpreting low-contrast scenes. Using the same data presented in the previous section, this enhanced thermal image (referred to as the eTherm image) is presented side-by-side with the standard thermal image. Note that only portions of the scene with a high degree of polarization are colorized whereas regions with low polarization automatically reduce to the same

grayscale value present in the standard thermal image. Most importantly, as polarization is dependent on the physics of the scene, the color scheme is necessarily consistent from frame to frame.

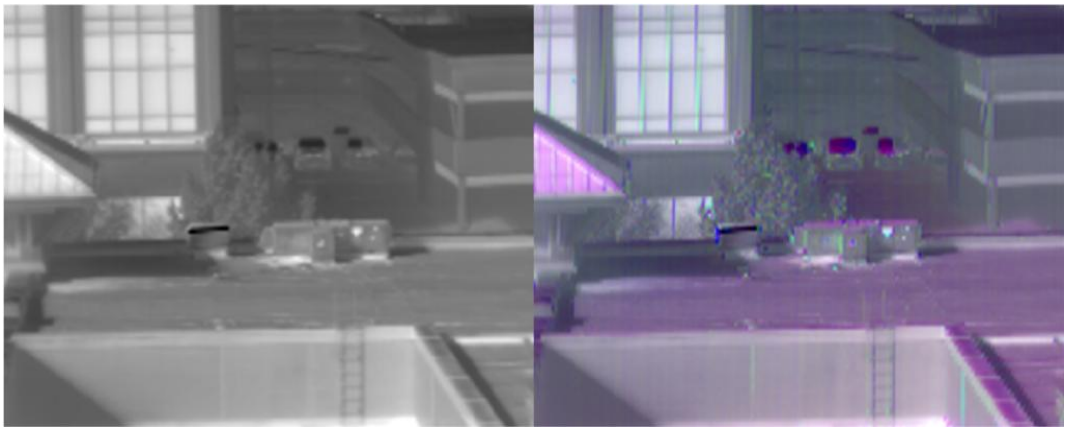

Figure 10. Vehicles at thermal equilibrium in standard thermal (left) and colorized eTherm image (right)

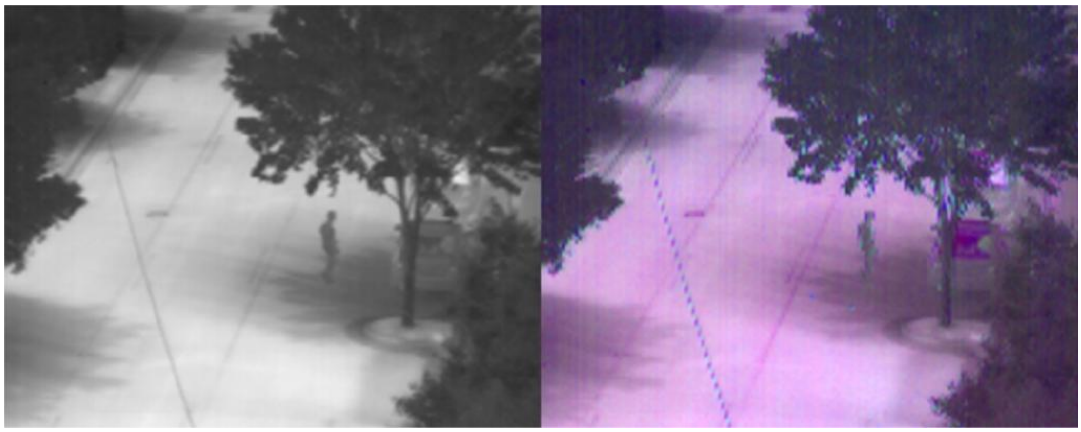

Figure 11. Pedestrian and vehicle shown standard thermal (left) and colorized eTherm image (right)

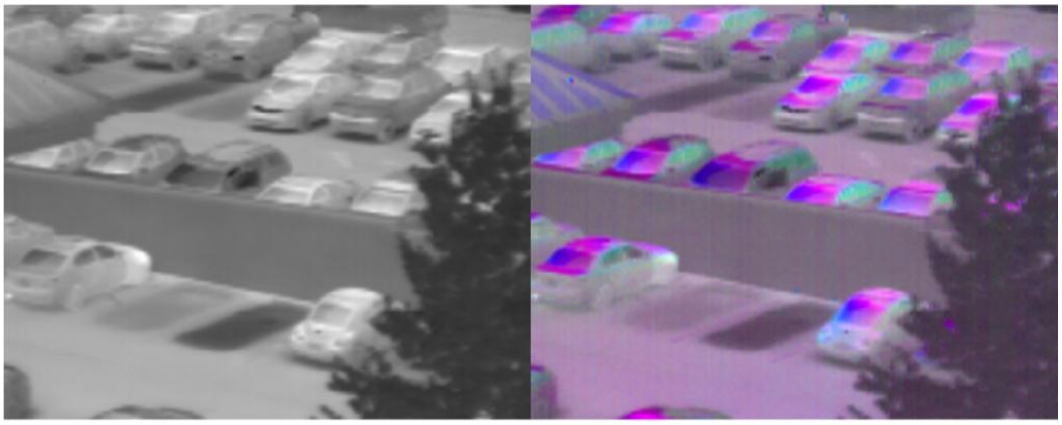

Figure 12. Parking lot in standard thermal (left) and colorized eTherm image (right)

Figure 13. Vehicles obscured by vegetation in standard thermal (left) and colorized eTherm image (right)

Figure 14. Train tracks and road way with extended shadow shown in standard thermal (left) and colorized eTherm image (right)

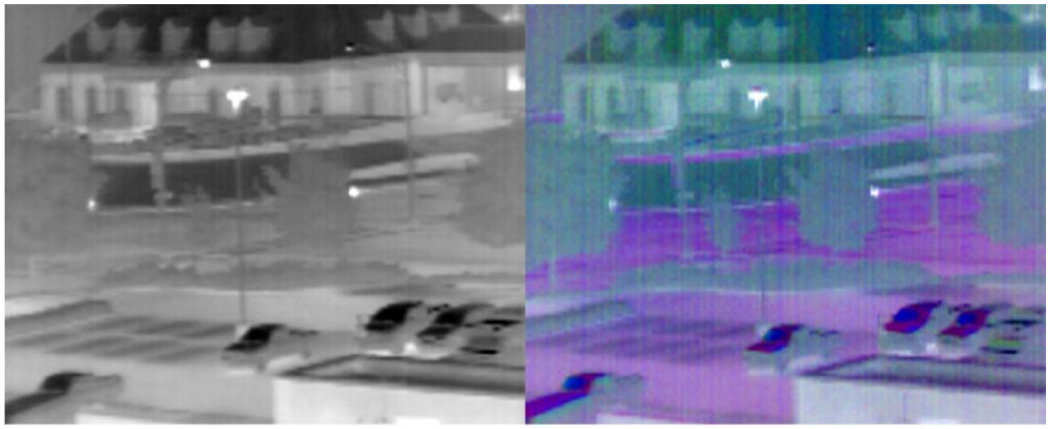

Figure 15. Low light cluttered scene shown in standard thermal (left) and colorized eTherm image (right)

6. CONCLUSION

This paper demonstrates the performance of passive LWIR imaging polarimetry as a robust method for clutter reduction in complex scenes. Use of a micro-bolometer based polarimeter demonstrates the applicability of this technology for use on unmanned systems due to the architecture's low SWaP-C. Because it is a physics-based detection scheme, infrared imaging polarimetry has been shown to be a robust approach for reducing scene clutter in IR imagery. The use of modern machine vision algorithms is well suited to simultaneously utilize each of the multiple polarimetric parameters (S_0, S_1, S_2, and DoLP), however the eTherm polarization-based coloring scheme has been shown to be ideal for man-in-the-loop applications. The results discussed in this paper may be achieved using any one of Polaris' COTS infrared imaging polarimeters and the particular choice of one versus another is mainly driven by practical constraints such as SWaP-C.

REFERENCES

[1] J. Tyo, D. Goldstein, D. Chenault, and J. Shaw, "Review of passive imaging polarimetry for remote sensing applications," Appl. Opt. 45, 5453-5469 (2006).

[2] Jacob L. Michalson ; Joao M. Romano ; Luz Roth; Stokes vector analysis of LWIR polarimetric in adverse weather. Proc. SPIE 8160, Polarization Science and Remote Sensing V, 81600N (September 9, 2011); doi:10.1117/12.893708.

[3] M. Felton ; K. P. Gurton ; J. L. Pezzaniti ; D. B. Chenault ; L. E. Roth; Comparison of the inversion periods for MidIR and LWIR polarimetric and conventional thermal imagery. Proc. SPIE 7672, Polarization: Measurement, Analysis, and Remote Sensing IX, 76720R (April 26, 2010); doi:10.1117/12.850264.

[4] Joao M. Romano ; Melvin Felton ; David Chenault ; Brian Sohr; Polarimetric imagery collection experiment. Proc. SPIE 7696, Automatic Target Recognition XX; Acquisition, Tracking, Pointing, and Laser Systems Technologies XXIV; and Optical Pattern Recognition XXI, 769611 (May 12, 2010); doi:10.1117/12.849911.

[5] Kristan Gurton ; Melvin Felton ; Robert Mack ; Daniel LeMaster ; Craig Farlow ; Michael Kudenov ; Larry Pezzaniti; MidIR and LWIR polarimetric sensor comparison study. Proc. SPIE 7672, Polarization: Measurement, Analysis, and Remote Sensing IX, 767205 (April 24, 2010); doi:10.1117/12.850341.

[6] John Harchanko ; David Chenault ; Craig Farlow ; Kevin Spradley; Detecting a surface swimmer using long wave infrared imaging polarimetry (Invited Paper). Proc. SPIE 5780, Photonics for Port and Harbor Security, 138 (May 25, 2005); doi:10.1117/12.603874.

[7] John S. Harchanko ; David B. Chenault; Water-surface object detection and classification using imaging polarimetry. Proc. SPIE 5888, Polarization Science and Remote Sensing II, 588815 (September 02, 2005); doi:10.1117/12.623542.

[8] Goldstein, D. *Polarized Light*. *2nd Edition*. New York City: Marcel Dekker, Inc. 2003. Print.

[9] Balanis, C. *Advanced Engineering Electromagnetics*. Hoboken, NJ: John Wiley & Sons, Inc. 1989. Print

[10] Hecht, E. *Optics. 4th Edition*. San Francisco: Pearson/Addison Wesley. 2002. Print.

[11] Michelson, A. A. *Studies in Optics*. Ontario: General Publishing Company, Ltd. 1995. Print.

[12] Christopher M. Persons ; Michael W. Jones ; Craig A. Farlow ; L. Denise Morell ; Michael G. Gulley ; Kevin D. Spradley; A proposed standard method for polarimetric calibration and calibration verification. Proc. SPIE 6682, Polarization Science and Remote Sensing III, 66820K (September 13, 2007); doi:10.1117/12.732137.